


Variable and Orbital-Dependent Spin-Orbit Field Orientations in an InSb Double Quantum Dot Characterized via Dispersive Gate Sensing

Lin Han,^{1,*} Michael Chan¹,¹ Damaz de Jong,¹ Christian Prosko¹,¹ Ghada Badawy,² Sasa Gazibegovic,² Erik P.A.M. Bakkers,² Leo P. Kouwenhoven,¹ Filip K. Malinowski,^{1,†} and Wolfgang Pfaff³

¹*QuTech and Kavli Institute of Nanoscience, Delft University of Technology, Delft 2600 GA, Netherlands*

²*Department of Applied Physics, Eindhoven University of Technology, MB Eindhoven 5600, Netherlands*

³*Department of Physics and Frederick Seitz Materials Research Laboratory, University of Illinois at Urbana-Champaign, Urbana, Illinois 61801, USA*

 (Received 1 April 2022; revised 26 October 2022; accepted 13 December 2022; published 24 January 2023)

Utilizing dispersive gate sensing (DGS), we investigate the spin-orbit field (\mathbf{B}_{SO}) orientation in a many-electron double quantum dot (DQD) defined in an InSb nanowire. While characterizing the interdot tunnel couplings, we find the measured dispersive signal depends on the electron-charge occupancy, as well as on the amplitude and orientation of the external magnetic field. The dispersive signal is mostly insensitive to the external field orientation when a DQD is occupied by a total odd number of electrons. For a DQD occupied by a total even number of electrons, the dispersive signal is reduced when the finite external magnetic field aligns with the effective \mathbf{B}_{SO} orientation. This fact enables the identification of \mathbf{B}_{SO} orientations for different DQD electron occupancies. The \mathbf{B}_{SO} orientation varies drastically between charge transitions, and is generally neither perpendicular to the nanowire nor in the chip plane. Moreover, \mathbf{B}_{SO} is similar for pairs of transitions involving the same valence orbital, and varies between such pairs. Our work demonstrates the practicality of DGS in characterizing spin-orbit interactions in quantum dot systems, without requiring any current flow through the device.

DOI: [10.1103/PhysRevApplied.19.014063](https://doi.org/10.1103/PhysRevApplied.19.014063)

I. INTRODUCTION

A spinful charge carrier moving in an electromagnetic field may experience a coupling between its spin and momentum degree of freedom, namely spin-orbit interaction (SOI). The SOI allows spin manipulation with electric fields in semiconductor platforms, such that it enables electric dipole spin resonance [1–4], spin-cavity couplings [5–8], while it also enhances effects detrimental to spin-based quantum information processing: relaxation and decoherence [9,10]. For many cases, SOI can be described as an effective spin-orbit field (\mathbf{B}_{SO}) acting on the charge carriers. Notably, \mathbf{B}_{SO} associated with the Rashba SOI is perpendicular to both the electric field \mathbf{E} and the carrier momentum \mathbf{p} , following $\mathbf{B}_{\text{SO}} \propto \mathbf{E} \times \mathbf{p}$ [11,12]. In ideal nanowire systems, carriers are confined in a one-dimensional path, which forces their momentum \mathbf{p} to be along the nanowire. With the application of bottom electrostatic gates, the assumed electric field \mathbf{E} is perpendicular to the substrate surface. Accordingly, the \mathbf{B}_{SO} orientation

is expected and has been experimentally proved to be not only in plane of the chip, but also nearly perpendicular to a bottom-gated nanowire [12,13]. Despite the electrostatic confinement, this conclusion is further found to hold for electron tunneling in few-electron double quantum dots (DQDs), even when the center-to-center distance between the dots is small with respect to typical spin-orbit lengths [14–16]. Knowing the \mathbf{B}_{SO} orientation in such nanowires is particularly useful for semiconductor-superconductor hybrid systems that aim to realize Majorana zero modes, as setting the external magnetic field perpendicular to \mathbf{B}_{SO} is a precondition to open a topological gap [17].

The conventional way to characterize SOI is associated with tunneling between quantum dots, which employs bias voltages across a DQD segment and measurements of spin-blockade leakage current [14,18–20]. However, scalable qubit devices [21,22] may favor characterization methods that do not require transport measurements. Here, we explore dispersive gate sensing (DGS) [8,23–28] to characterize SOI, especially the \mathbf{B}_{SO} orientation. Our protocol does not employ transport measurements, is compatible with fast data acquisition in rastering schemes [25,29], and is promising for the integration of qubit characterization and readout capabilities [30,31].

*L.Han-2@tudelft.nl

†F.K.Malinowski@tudelft.nl

II. METHOD

In this section, we present the fabrication details of the device and the principal of the measurements (Sec. II A). At zero magnetic field, the measured charge diagram via DGS helps on charge-parity recognition, and its result is evidenced by the data under finite external magnetic field (Sec. II B). The conversion of measured reflection coefficients to quantum capacitance C_q follows (Sec. II C), which is the basis of identifying spin-orbit field orientations for even total parity.

A. Device and measurement approach

The device under study is depicted in Fig. 1(a). An InSb nanowire is placed on top of prefabricated bottom finger gates. The barrier gates confine the electrons and control the tunnel coupling within the DQD and to the leads, while the plunger gates LP (RP) tune the chemical potential of the left (right) dot. The nanowire is grown along [111] direction, such that the Rashba SOI is expected to be dominant [13,14,32]. To implement DGS, the RP gate is coupled to an off-chip superconducting spiral-inductor resonator, with resonance frequency $f_0 \approx 318.4$ MHz and nominal inductance $L = 730$ nH [33].

At interdot charge transitions (ICTs), where the chemical potential for an electron residing in the left and the right dot are equal, the hybridization of electron wave functions between the two dots leads to an additional quantum capacitance C_q loading the resonator, which is observable as a shift of f_0 [23,25,34,35]. While fixing the probing frequency f_p and detecting the reflected signal from the resonator, f_0 is translated into a change of reflection coefficient, thus to the amplitude and phase response. We fit the measured reflection coefficient with an analytical resonator model to extract f_0 and C_q (see Sec. II C). All measurements are performed in a dilution refrigerator at a base temperature $T \approx 30$ mK.

B. Recognition of charge parity

In Fig. 1(b), the charge-stability diagram (CSD) of the DQD is mapped by measuring the reflected phase response versus gate voltages V_{LP} and V_{RP} . It reveals a grid of ICTs with the lead-to-dot transitions hardly visible (marked by white lines), since the outer barrier gates are nearly pinched off. Along V_{LP} and V_{RP} axes, both the spacings between the ICTs and the measured phase shifts at the ICTs tend to alternate between smaller and larger values [inset of Fig. 1(b)]. As loading every other additional electron requires compensating for the level spacing on top of the charging energy, the smaller spacings along V_{LP} (V_{RP}) are associated with having an odd number of electrons in the left (right) dot [36]. Furthermore, an ICT corresponding to a total odd number of electrons in the DQD exhibit a larger phase shift, since the spin degeneracy of having

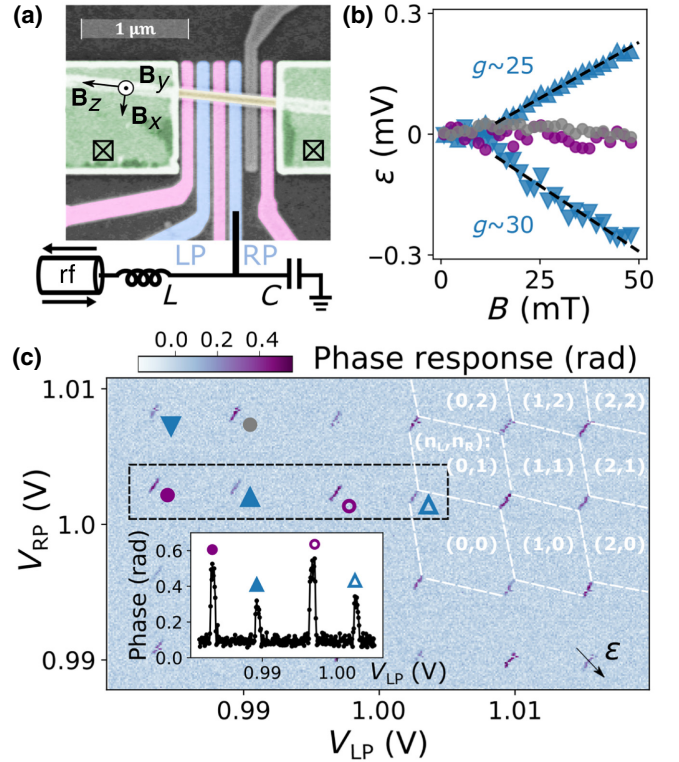


FIG. 1. (a) False-colored SEM image of the device and the circuit schematics for DGS. The barrier and plunger gates are indicated in pink and blue, respectively, while the metallic leads are indicated in green. The gray gate is electrostatically floating (unused in this work). (b) Charge-stability diagram of the DQD at zero magnetic field. The inset shows the maximum phase response in the V_{LP} range marked by the dashed black rectangle. (c) The position of four neighboring ICTs along detuning axis, as a function of external field pointing in an arbitrary direction. Markers in (b) indicate the relative charge occupancy of the ICTs, although they do not correspond to the same ICTs as in (c).

total even charges leads to a reduction of the maximum of C_q [4,26,37].

The identification of the total charge parity in the DQD is additionally verified by applying an external magnetic field \mathbf{B} [Fig. 1(c)] [38]. For four neighboring ICTs, their positions along the detuning axis are measured as a function of \mathbf{B} , with detuning $\varepsilon := [(V_{LP} - V_{LP,\varepsilon=0}) - (V_{RP} - V_{RP,\varepsilon=0})]/2$. We observe shifts only for the ICTs with a total even occupancy, consistent with Zeeman effect. Fits to the data for even-occupied ICTs in a region exhibiting a linear shift in magnetic field [4] yield the effective g factors of approximately 25 and 30. Based on these observations, the parity of the electron numbers in the DQD is indicated with labels (n_L, n_R) , with $n_{L(R)}$ indicating the excess number of electrons with respect to an even number of electrons (N_L, N_R) on the left (right) dot [also indicated in Fig. 1(b)]. The number of electrons in each dot is estimated to be in the range of 70 to 150 electrons, considering the plunger

gate voltages, pinch off voltages, and the spacing between ICTs.

C. Extraction of quantum capacitance

Quantum capacitance C_q is extracted by calculating the changes of the capacitive load on the resonator from its bare value C_{cb} , as this results in a resonance frequency shift Δf that is directly obtainable from measurements [25]:

$$C_q = C - C_{cb} = \frac{1}{(2\pi)^2(f_{cb} + \Delta f)^2 L} - \frac{1}{(2\pi)^2 f_{cb}^2 L}. \quad (1)$$

Here, C is the effective capacitance being measured, L is fixed to be 730 nH. C_{cb} and f_{cb} are the capacitance and resonance frequency at Coulomb blockade, respectively. According to this equation, the values of f_{cb} and Δf are required to get C_q .

The measurement of C_q at given gate settings under a certain external magnetic field consists of two steps. In the first step, we fix the gate settings near the ICT that we aim to study, and measure the frequency dependence of the reflection coefficient S_{11} around the resonance frequency f_0 [e.g., Fig. 2(a)]. The measurement result is regarded as a reference data. Considering the hanger geometry of the coupled resonator, we fit the measured S_{11} with the resonator model inspired by Khalil *et al.* [39], where they derive the transmission coefficient S_{21} of the hanger resonator. At probing frequency f_p , the measured S_{11} differs from S_{21} by a factor of 2 to convert from transmission to reflection:

$$S_{11} = 1 - \frac{2e^{i\Phi} \frac{Q}{Q_e}}{1 + 2iQ \frac{f_p - f_0}{f_0}}. \quad (2)$$

Here, $Q = 1/(1/Q_i + 1/Q_e)$ is the total quality factor, with $Q_{i(e)}$ being the internal (external) quality factor [26,40]. The asymmetry of reflection is captured by the phenomenological phase term $e^{i\Phi}$, while is originated from the impedance mismatch as in Ref. [39]. Therefore, we obtain the value of f_0 for that particular gate setting, and the corresponding parameters of the resonator, including $Q_{i(e)}$, and phase factor Φ . With this approach, the values of quality factors are not accurately defined, but the influence on analysis is negligible when they are fixed in our case. Figures 2(a) and 2(b) show an example of the fitting results compared to the raw data in both amplitude response and in I - Q plane. In the second step, we fix the probing frequency to f_p , and measure the CSD that completely encompasses the target ICT [see Fig. 2(c)].

We assume all resonator parameters collected from the reference data to be fixed within the gate-voltage space of that CSD, except for C_q that changes the resonance frequency by Δf . As the probing frequency f_p is known, for each pixel i in the CSD [e.g., in Fig. 2(c)], we convert all

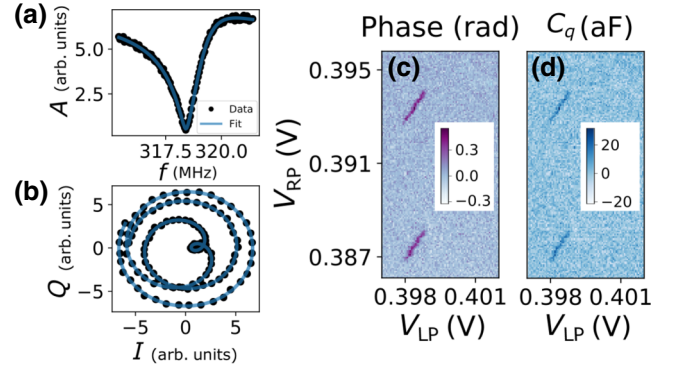


FIG. 2. (a) The magnitude of the reflection signal as a function of probing frequency, as an example of the reference data. The black dots represents the raw data, while the blue curve shows the fitting result. (b) Parametric plot of the resonator reflection measurement in I - Q plane, and the corresponding fit result. (c) The reflected phase signal of the entire CSD. (d) The corresponding color maps of C_q values.

the measured S_{11}^i into different resonance frequencies f_0^i , according to the resonator model in Eq. (2) with the fitted resonator parameters. The value of f_{cb} is defined as a mean value of the resonance frequency f_0^i away from any ICT. This means that the resonance frequency shifts Δf^i are defined relative to f_{cb} . Finally, with Eq. (1), the values of C_q^i in the scanned gate-voltage space are extracted, as shown in Fig. 2(d).

III. IDENTIFICATION OF SPIN-ORBIT FIELD ORIENTATION

Having identified the total charge parity of the ICTs, we characterize the \mathbf{B}_{SO} field orientation for an even-occupied ICT. We apply an external magnetic field with fixed amplitude $|\mathbf{B}| = 30$ mT. $C_{q,max}$, which denotes the maximum values of C_q at the ICT, is extracted as a function of the field orientation in spherical coordinates φ and θ [Fig. 3(a)]. Figures 3(d) and 3(e) display the obtained data in range $0^\circ \leq \theta \leq 90^\circ$, and $90^\circ \leq \theta \leq 180^\circ$, respectively. There are two regions at which $C_{q,max}$ is strongly suppressed. They lie at opposite directions in the spherical coordinates, neither perpendicular to the nanowire, nor in plane of the substrate. We interpret the centers of the suppression regions as corresponding to the directions parallel and antiparallel to \mathbf{B}_{SO} . Energy diagrams of the DQD are presented in Figs. 3(b) and 3(c). Due to different total spin, the lowest singlet state $|S(2, 0)\rangle$ and triplet state $|T_+(1, 1)\rangle$ only couple if electron spin flips during tunneling are allowed. This coupling arises only when \mathbf{B} is not aligned with \mathbf{B}_{SO} [Fig. 3(b)], resulting in finite curvature of the ground-state energy at the ICT, and thus finite $C_{q,max}$. When $\mathbf{B} \parallel \mathbf{B}_{SO}$, the two states do not couple [Fig. 3(c)], therefore $C_{q,max}$ is suppressed because of the flat energy dispersion of $|T_+(1, 1)\rangle$ state [4,41,42].

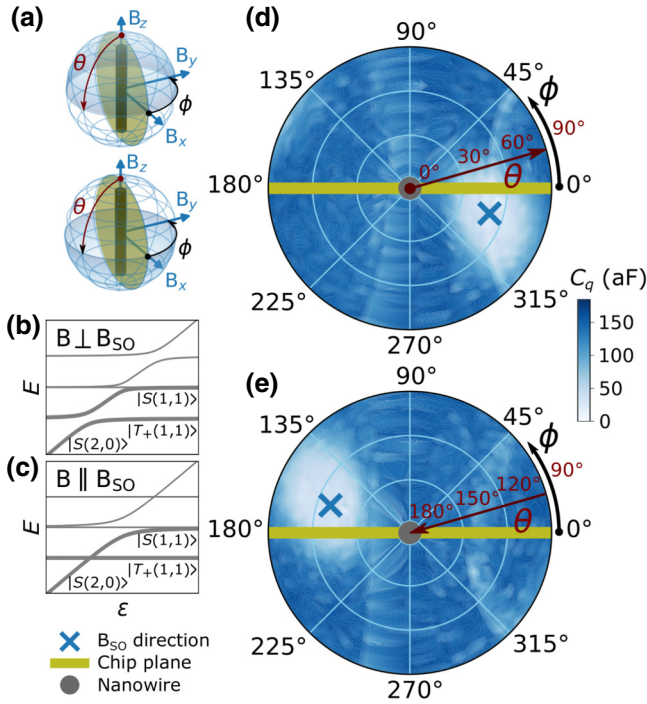


FIG. 3. (a) Illustration of spherical coordinates with respect to the nanowire and the substrate. The top and bottom panel correspond to (d),(e), respectively. (b),(c) Schematic energy diagrams of a DQD for (b) $\mathbf{B} \perp \mathbf{B}_{\text{SO}}$ and (c) $\mathbf{B} \parallel \mathbf{B}_{\text{SO}}$. The (avoided) crossing between the two lowest states are highlighted. $C_{q,\text{max}} = 0$ when they cross, due to the flat shape of $|T_+(1,1)\rangle$. (d),(e) The extracted $C_{q,\text{max}}$ values plotted on an external magnetic field angle map. Polar projection of the map is shown in (d) when $0^\circ \leq \theta \leq 90^\circ$, and (e) when $90^\circ \leq \theta \leq 180^\circ$. The blue crosses mark the characterized $\pm \mathbf{B}_{\text{SO}}$ orientations, which is the center of the region where $C_{q,\text{max}}$ is suppressed.

The observation that \mathbf{B}_{SO} is neither perpendicular to the nanowire nor in plane of the chip can be attributed to several reasons. First, the complicated gate structure is likely to create a nonuniform potential, making the local electric fields deviate significantly from the out-of-plane direction. Second, staying in many-electron regime brings more complexity, as the overlap between the wave functions of the two dots may not spatially coincide with the direction of the nanowire. Consequently, the momentum associated with electron tunneling is not necessarily along the nanowire. Third, although not dominant, a finite contribution of Dresselhaus SOI may also exist, so that spin modulations in the cross-section plane contribute to the offset angle with respect to the chip plane [43].

IV. EXTERNAL FIELD DEPENDENCE OF QUANTUM CAPACITANCE

Next, we study the evolution of C_q at the same ICT, as a function of \mathbf{B} and ϵ . While increasing the amplitude of $\mathbf{B} \perp \mathbf{B}_{\text{SO}}$, we find a nearly linear shift of the C_q maximum

along detuning axis [Figs. 4(a) and 4(b)]. This is accompanied by a gradual increase of $C_{q,\text{max}}$ value [Fig. 4(c)], starting at about 100 aF when \mathbf{B} is zero, and saturating near 150 aF for \mathbf{B} above 25 mT. In contrast, $C_{q,\text{max}}$ is suppressed [Figs. 4(d)–4(f)] for $\mathbf{B} \parallel \mathbf{B}_{\text{SO}}$, since \mathbf{B}_{SO} no longer introduces singlet-triplet coupling in this orientation. Along \mathbf{B}_{SO} , the suppression occurs in two distinct steps [see Fig. 4(f)]. Initially, $C_{q,\text{max}}$ drops rapidly from 100 aF for low \mathbf{B} , and starts saturating near the value of 50 aF with \mathbf{B} above approximately 10 mT. Then, $C_{q,\text{max}}$ starts dropping even further at about 25 mT. In the limited measurement range, $C_{q,\text{max}}$ appears to be trending towards zero.

To understand the capacitive response of the ICT in magnetic field, we employ a two-site Hubbard model (see Appendix) [44]. The SOI in our model is phenomenologically described as an effective field, which can point in an arbitrary direction in space, namely both Rashba and Dresselhaus SOI are taken into consideration. The model includes the spin precessing tunneling matrix element t_p as part of total tunneling strength t_{tot} . The term t_p depends on the SOI strength and modulates spin-flip together with the angle between \mathbf{B} and \mathbf{B}_{SO} . The individual cuts at $B = 0$ and $B = 50$ mT for $\mathbf{B} \perp \mathbf{B}_{\text{SO}}$ are used to estimate $t_{\text{tot}} = 20 \mu\text{eV}$ and $t_p = 18 \mu\text{eV}$, by fitting the analytical expressions of C_q in the Appendix. For simplicity, we assume isotropic g factors $g = 32$ being equal in both dots, with the value taken from linear shifts of charge transitions in Fig. 4(a). The effective lever arm of the gate attached to the resonator is $\alpha = 0.26$, according to the ratio between the height and width of a Coulomb diamond, and an estimated crosstalk between the gates of 20%. The electron temperature in the model is set to 30 mK, based on a Coulomb blockade thermometry measurement performed before this experiment. The simulated results are illustrated in the insets of Figs. 4(a) and 4(d), and in black in Figs. 4(b), 4(c), 4(e), and 4(f). For $\mathbf{B} \perp \mathbf{B}_{\text{SO}}$, we find an excellent agreement with the data in a full range of magnetic fields, with no free parameters. In contrast, for $\mathbf{B} \parallel \mathbf{B}_{\text{SO}}$, the simulated shift of the ICT along detuning axis is greater than observed when \mathbf{B} is below 25 mT. Furthermore, the model does not qualitatively capture the two-stage suppression of $C_{q,\text{max}}$ when \mathbf{B} increases [Fig. 4(f)].

We identify two elements in our model potentially responsible for the discrepancy. First, we consider possible g factor nonuniformity and anisotropy [14,45,46]. In particular, a smaller g factor for $\mathbf{B} \parallel \mathbf{B}_{\text{SO}}$ can reduce the shift in detuning of the ICT in Fig. 4(d), and eventually increase \mathbf{B} at which the predicted suppression of $C_{q,\text{max}}$ occurs. Second, when $\mathbf{B} \parallel \mathbf{B}_{\text{SO}}$, spin relaxation rates mediated by hyperfine and SOI are hindered [47,48]. As a consequence, Pauli spin-blockade traps the system in one of the excited states, which do not contribute to $C_{q,\text{max}}$. We hypothesize that unaccounted Pauli spin blockade is responsible for the suppression of the $C_{q,\text{max}}$ in the range of 0–25 mT.

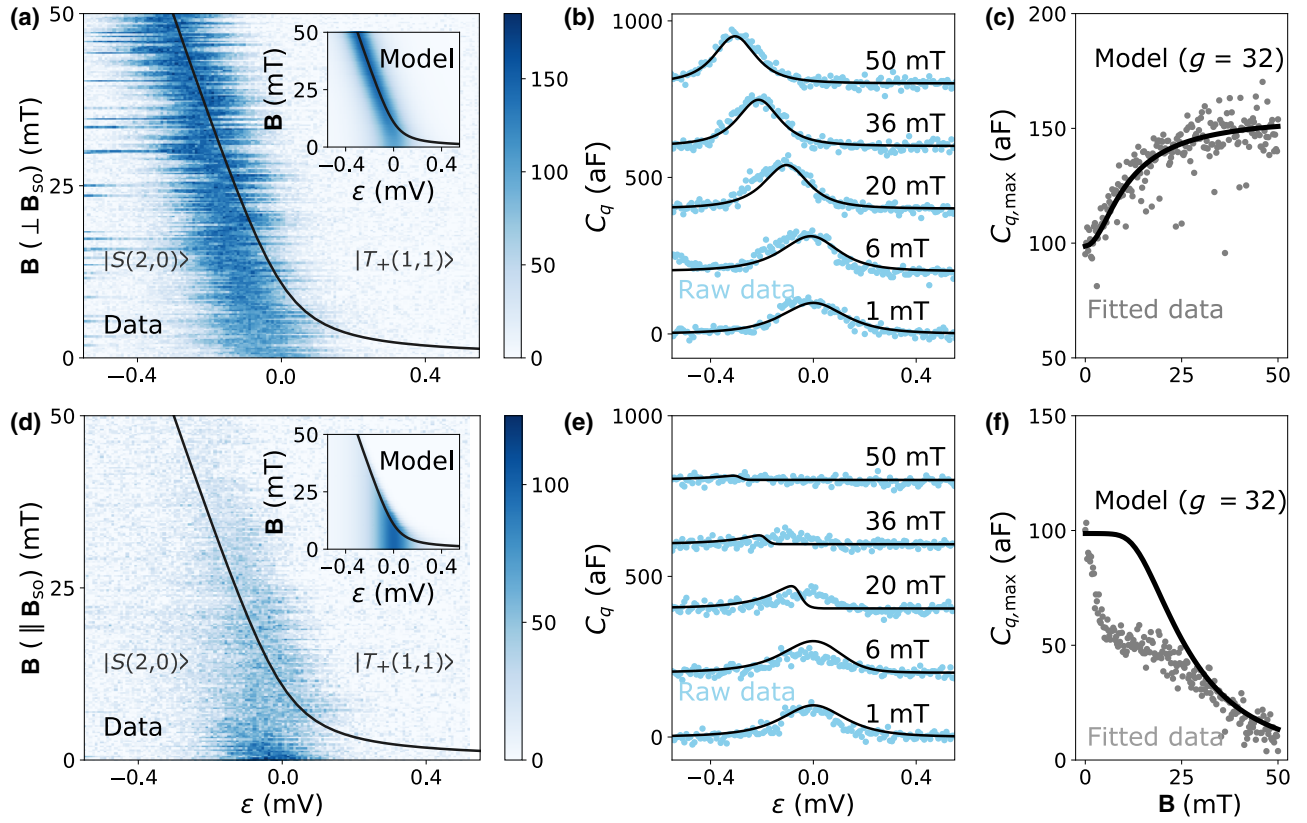


FIG. 4. Evolution of the ICT in external magnetic field \mathbf{B} for (a)–(c) $\mathbf{B} \perp \mathbf{B}_{\text{SO}}$, and (d)–(f) $\mathbf{B} \parallel \mathbf{B}_{\text{SO}}$. (a),(d) C_q as a function of \mathbf{B} and ϵ . The inset presents the numerical simulation. Black curves in both the main figure and the inset indicate the degeneracy point between $|S(2,0)\rangle$ and $|T_+(1,1)\rangle$. (b),(e) Line cuts of (a),(d) for several magnitudes of \mathbf{B} . For clarity, they are separated in the C_q axis by 200 aF. Black curves come from the simulation. (c),(f) $C_{q,\text{max}}$ as a function of \mathbf{B} . Gray dots are extracted from a phenomenological Gaussian fit of the data. Black curves indicate the $C_{q,\text{max}}$ taken from the insets of (a),(d).

Meanwhile, the $C_{q,\text{max}}$ suppression above 25 mT is consistent with our model, except it occurs at higher field due to an overestimated g factor. This can be identified from comparing the C_q peaks of model and data in Fig. 4(e).

V. VARIATIONS OF SPIN-ORBIT FIELD ORIENTATION

After analyzing an individual ICT, we look into the \mathbf{B}_{SO} orientation of clusters of ICTs. Specifically, in the gate-voltage space along V_{LP} and V_{RP} , we study a 4-by-4 array of neighboring ICTs [see Figs. 5(a)–5(p)], and exhibit them in the same order as in the CSD in Fig. 1(c). We rotate \mathbf{B} with fixed amplitude of 50 mT while measuring $C_{q,\text{max}}$ for those neighboring ICTs, where for odd-occupied ICTs, the extracted $C_{q,\text{max}}$ is independent of the \mathbf{B} orientation. In contrast, the majority of even-occupied ICTs show a fairly well-defined direction in which $C_{q,\text{max}}$ is suppressed, indicating the orientation of \mathbf{B}_{SO} . A few of the ICTs reveal a $C_{q,\text{max}}$ suppression in a peculiar pattern with no clear preferred direction [e.g., Figs. 5(a) and 5(f)], which will be discussed later.

Figure 5(q) summarizes all of the extracted \mathbf{B}_{SO} orientations, including some cases where we tune the barrier and plunger gates by a large amount. The crosses with the same color indicate pairs of ICTs of the same valence orbital. For three such ICT pairs, the corresponding maps of extracted $C_{q,\text{max}}$ with colored crosses are presented in Figs. 5(a)–5(p). Blue squares in (q) indicate the ICTs for which the other ICT from a pair is not measured. Because of the inversion symmetry shown in Figs. 3(d) and 3(e), only the measurements for $0^\circ \leq \theta \leq 90^\circ$ are performed.

The markers in Fig. 5(q) show no preferred direction among the complete set of measured \mathbf{B}_{SO} orientations. Notably, for a pair of ICTs corresponding to the same valence orbital, their \mathbf{B}_{SO} orientations are much closer to each other than to other random pairs. This thereby supports the hypothesis that the random orientation of \mathbf{B}_{SO} arises from the complex shape of the electronic orbitals and the hard-to-predict local \mathbf{E} . Imperfect alignment of the \mathbf{B}_{SO} orientations within a pair of ICTs might be a consequence of a slight distortion of the confining potential, when the gates are tuning the dot occupancies. The irregular shape of the $C_{q,\text{max}}$ suppression regions for some of the ICTs [e.g.,

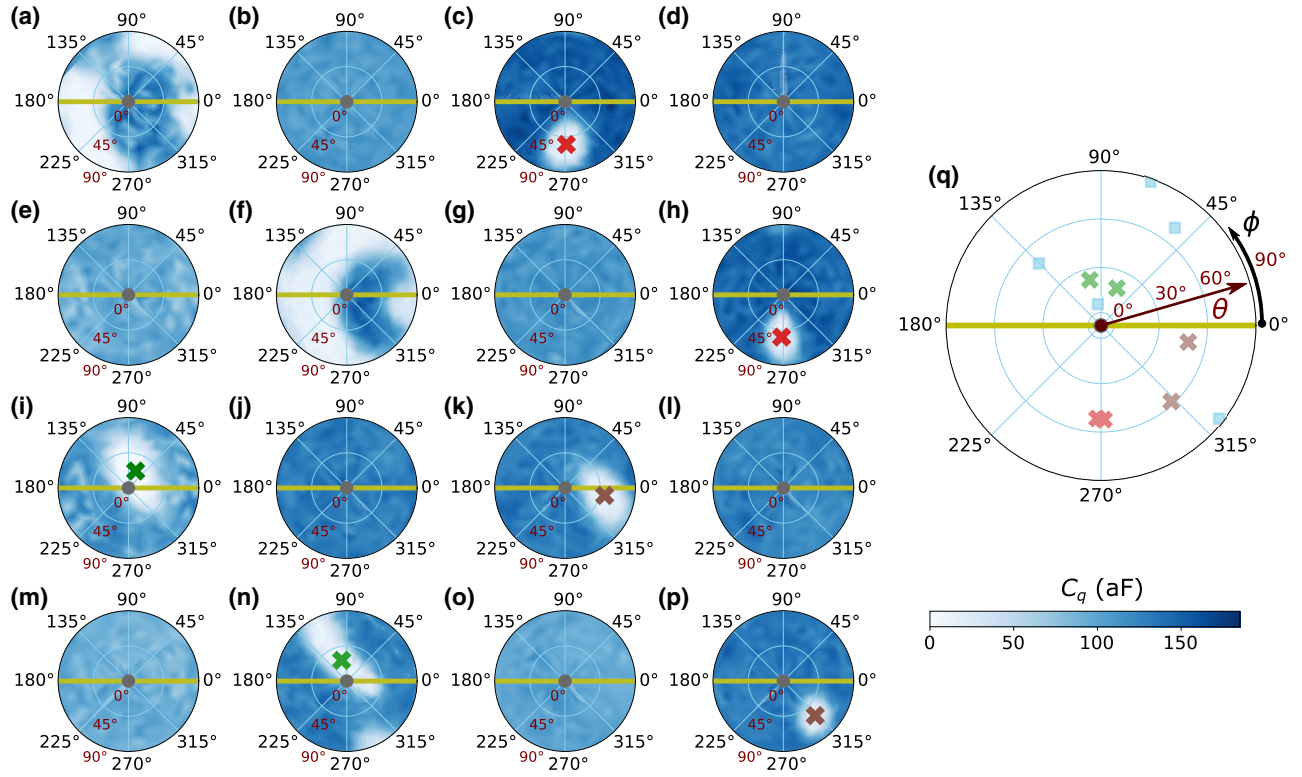


FIG. 5. (a)–(p) The external magnetic field angle map of $C_{q,\max}$ ($0^\circ \leq \theta \leq 90^\circ$, with $|\mathbf{B}| = 50$ mT) for 16 neighboring ICTs, with their extracted \mathbf{B}_{SO} directions marked by colored crosses. These ICTs are labeled with the corresponding charge occupations (n'_L, n'_R) with respect to even charge numbers (N'_L, N'_R). (q) Summary of the extracted \mathbf{B}_{SO} directions for the even-occupied ICTs under study. Crosses in the same color correspond to the ICT pairs with the same valence orbital. Squares mark the ICTs when the other ICT from a pair is not measured.

Figs. 5(a), 5(f), and 5(n)] demonstrates that the description of SOI in terms of effective \mathbf{B}_{SO} and isotropic g factors is incomplete.

In Ref. [49], Scheübl *et al.* discuss the topological nature of Weyl points between the lowest singlet and triplet states, which is equivalently manifested by the suppression of C_q in our experiment. They show that the number of such Weyl points is not restricted to be two [like in Figs. 3(d) and 3(e)], but may be six or even larger for rare cases. The presence of more than two Weyl points might explain the highly irregular regions of $C_{q,\max}$ suppression for some ICTs. The $C_{q,\max}$ suppression regions in Figs. 5(a) and 5(f) are too large to fit \mathbf{B}_{SO} orientations meaningfully, which may be due to a small level spacing to the first excited state.

VI. SUMMARY

In summary, we study \mathbf{B}_{SO} orientation using DGS in an InSb nanowire-based DQD. At zero magnetic field, DGS can be employed as a charge-parity meter, and ICTs with even total parity are identified for further \mathbf{B}_{SO} characterization. When a finite external field \mathbf{B} is rotated, the

directions in which $C_{q,\max}$ is suppressed reveal the \mathbf{B}_{SO} orientation of even-occupied ICTs. We model the dispersive signal at an even-occupied ICT, and find good agreement with the data for $\mathbf{B} \perp \mathbf{B}_{\text{SO}}$. However, for $\mathbf{B} \parallel \mathbf{B}_{\text{SO}}$, our model lacks a description of the suppressed spin relaxation rates due to Pauli blockade. Finally, we find that \mathbf{B}_{SO} for the ICT pairs with the same valence orbital have similar orientations, while the \mathbf{B}_{SO} orientation varies enormously between different orbitals. Our work indicates that considerations about \mathbf{B}_{SO} orientation based purely on device design may often not apply to quantum dot systems. Resolving whether the randomness of \mathbf{B}_{SO} orientation persists in quantum devices, either based on nanowires or two-dimensional electron gases, is essential to assess the viability of different materials for quantum computing with spins and Majorana zero modes. Moreover, DGS is shown to be an effective tool in characterizing the \mathbf{B}_{SO} orientation, especially when transport measurements are not applicable. This result also broadens the prospects for systems applying DGS that feature integrated capabilities for qubit characterization and readout, while avoiding increasing the complexity in the chip design [30,31,50].

ACKNOWLEDGMENTS

We appreciate J. Koski for suggestions regarding to the experiment and the paper. We thank K. Li for assisting nanowire deposition, F. Borsoi, N. van Loo, and J. Wang for useful advice on fabrication, A. Palyi and Z. Scherübl for fruitful discussions on the measurement results, also M. Hornibrook and D.J. Reilly for providing the frequency multiplexing chips, O.W.B. Benningshof, R.N. Schouten, and J.D. Mensingh for valuable technical assistance. This work has been supported by the Netherlands Organization for Scientific Research (NWO) and Microsoft Quantum Lab Delft. F.K.M. acknowledges support from NWO under Veni Grant (VI.Veni.202.034).

APPENDIX: MODELING THE DQD

In order to describe the effects observed in the DQD, we construct an effective Hamiltonian \hat{H}_{tot} for the system in the Hund-Mulliken approximation using the second quantization notation [51,52]. Only one orbital per dot, which can be doubly occupied by electrons, is considered in this approximation. In our model, \hat{H}_{tot} consists of an electrostatic term \hat{H}_e , a magnetic Zeeman term \hat{H}_m and a SOI term \hat{H}_{SO} :

$$\hat{H}_{\text{tot}} = \hat{H}_e + \hat{H}_m + \hat{H}_{\text{SO}}. \quad (\text{A1})$$

Formally, SOI mixes the orbital and spin part of the electron wave function, and results in Kramers doublets. They are referred to as the conventional spin doublets: an external magnetic field \mathbf{B} induces a Zeeman splitting between the spin doublets. The SOI itself is modeled as an effective electron momentum dependent magnetic field \mathbf{B}_{SO} , around which the spin of the tunneling electron precesses [14]. We use a phenomenological interaction Hamiltonian of the form of

$$\hat{H}_{\text{SO}} = \mathbf{B}_{\text{SO}}(\hat{p}_x, \hat{p}_y, \hat{p}_z) \cdot \hat{\sigma}, \quad (\text{A2})$$

where \hat{p}_i is the momentum operator in the three Cartesian directions ($i = x, y, z$), and $\hat{\sigma}$ is the Pauli (spin-1/2) operators. In particular, we define the spin basis of the electron such that the spin quantization axis (the projection of the spin on z axis) aligns with \mathbf{B} . The angle η is defined as the angle associated with the inner product of \mathbf{B} and \mathbf{B}_{SO} , allowing us to decompose \mathbf{B}_{SO} into a parallel and perpendicular component with respect to the spin quantization axis. For simplicity, we choose the projection of the spin on the y axis align with the component of \mathbf{B}_{SO} that is perpendicular to \mathbf{B} . The SOI Hamiltonian is, therefore, given as

$$\begin{aligned} \hat{H}_{\text{SO}} = it_p \sum_{\alpha, \beta = \{\uparrow, \downarrow\}} & \left(\cos(\eta) \hat{c}_{L, \alpha}^\dagger \hat{\sigma}_z^{\alpha\beta} \hat{c}_{R, \beta} \right. \\ & \left. + \sin(\eta) \hat{c}_{L, \alpha}^\dagger \hat{\sigma}_y^{\alpha\beta} \hat{c}_{R, \beta} - \text{h.c.} \right), \end{aligned} \quad (\text{A3})$$

where t_p is the spin precessing tunnel coupling due to SOI, while $\sigma_{y(z)}$ is the spin-1/2 Pauli y (z) matrices. $\hat{c}_{i, \sigma}^\dagger$ and $\hat{n}_{i, \sigma}$ are the fermionic creation and number operator for the electrons in dot i with spin σ .

Together with

$$\begin{aligned} \hat{H}_e = \frac{\epsilon}{2} \sum_{\sigma, \sigma' = \{\uparrow, \downarrow\}} & (\hat{n}_{L, \sigma} - \hat{n}_{R, \sigma'}) \\ & + t \sum_{\sigma} (\hat{c}_{L, \sigma}^\dagger \hat{c}_{R, \sigma} + \text{h.c.}) \\ & + \sum_{i = \{L, R\}} (U_i \hat{n}_{i, \uparrow} \hat{n}_{i, \downarrow}), \end{aligned} \quad (\text{A4})$$

and

$$\begin{aligned} \hat{H}_m = -\frac{\mu_B B}{2} (g_L (\hat{n}_{L, \uparrow} - \hat{n}_{L, \downarrow}) \\ + g_R (\hat{n}_{R, \uparrow} - \hat{n}_{R, \downarrow})), \end{aligned} \quad (\text{A5})$$

we obtain the full Hamiltonian of the DQD system. Here, ϵ is the detuning, t is the spin-conserving tunnel coupling, and $U_{L(R)}$ is the Coulomb repulsion induced energy cost for placing two electrons on the same left (right) dot. Moreover, μ_B denotes the Bohr magneton, B the external field magnitude, and $g_{L(R)}$ the Landé g factor of the left (right) dot.

For ICTs between the $|2, 0\rangle$ and $|1, 1\rangle$ charge states, the following even parity states are of relevance:

$$\begin{aligned} |2, 0\rangle_S &= \hat{c}_{L, \uparrow}^\dagger \hat{c}_{L, \downarrow}^\dagger |0\rangle \\ |1, 1\rangle_S &= \frac{1}{\sqrt{2}} (\hat{c}_{L, \uparrow}^\dagger \hat{c}_{R, \downarrow}^\dagger - \hat{c}_{L, \downarrow}^\dagger \hat{c}_{R, \uparrow}^\dagger) |0\rangle \\ |T_+\rangle &= \hat{c}_{L, \uparrow}^\dagger \hat{c}_{R, \uparrow}^\dagger |0\rangle \\ |T_0\rangle &= \frac{1}{\sqrt{2}} (\hat{c}_{L, \uparrow}^\dagger \hat{c}_{R, \downarrow}^\dagger + \hat{c}_{L, \downarrow}^\dagger \hat{c}_{R, \uparrow}^\dagger) |0\rangle \\ |T_-\rangle &= \hat{c}_{L, \downarrow}^\dagger \hat{c}_{R, \downarrow}^\dagger |0\rangle, \end{aligned} \quad (\text{A6})$$

with $|0\rangle$ being a vacuum state.

For $B = 0$, we can project \hat{H}_{tot} onto this basis and analytically diagonalize the Hamiltonian to find the ground-state energy

$$E_g = \frac{1}{2} ((U_L + \epsilon) - \sqrt{(U_L + \epsilon)^2 + 8(t^2 + t_p^2)}). \quad (\text{A7})$$

Note that U_L offsets (the onset of) the avoided crossing along the detuning axis only and can be set to zero by redefining the detuning axis. The C_q value can then be calculated as the curvature of the ground-state energy $-(e\alpha')^2 \partial^2 E_g / \partial \epsilon^2$, for which we find (α' is the effective

lever arm accounted for cross-coupling) [34,35,53]

$$C_{q,B=0} = \frac{(e\alpha')^2}{2} \frac{8t_{\text{tot}}^2}{(\epsilon^2 + 8t_{\text{tot}}^2)^{3/2}}, \quad (\text{A8})$$

where e is the elementary charge. In addition, we define $t_{\text{tot}} = \sqrt{t^2 + t_p^2}$ as the total tunnel coupling set by the barrier gates.

Another special limit is when $\mathbf{B} \perp \mathbf{B}_{\text{SO}}$, where $\eta = \pi/2$. According to \hat{H}_{SO} , the spin flipping due to SOI during tunneling is strongest. When the Zeeman energy E_z is the second largest energy scale ($E_z \gg t_{\text{tot}}$), we expect that the ground state is solely contributed to by the states $|(2, 0)S\rangle$ and $|T_+\rangle$ that are coupled by SOI through the tunneling element t_p . In this case, the ground and first excited state are analytically approximated by projecting \hat{H}_{tot} onto the aforementioned two states. The ground-state energy and C_q are found as

$$E_g = \frac{1}{2} \left[U_L + \epsilon - \frac{\mu_B B}{2} (g_L + g_R) - \sqrt{\left(U_L + \epsilon + \frac{\mu_B B}{2} (g_L + g_R) \right)^2 + 4t_p^2} \right];$$

$$C_{q,B \perp B_{\text{SO}}} = \frac{2(e\alpha')^2 t_p^2}{\left[(U_L + \epsilon + \frac{\mu_B B (g_L + g_R)}{2})^2 + 4t_p^2 \right]^{3/2}}. \quad (\text{A9})$$

For the more general case, we employ numerical simulations to compute C_q . We project the five spin basis states [in Eq. (A6)] onto \hat{H}_{tot} and numerically diagonalize it to find the eigenenergies E_n and states Ψ_n . In the limit of relaxation rates being slower than the probing frequency, C_q is calculated as the curvature of the energy bands, or equivalently through $(e\alpha')^2 d\langle n_L \rangle / d\epsilon$ [41]. In thermal equilibrium, C_q can be expressed as

$$C_q = (e\alpha')^2 \sum_n \frac{e^{-E_n(\epsilon)/k_B T}}{\mathcal{Z}} \left(\frac{d\langle \Psi_n | \hat{n}_L | \Psi_n \rangle(\epsilon)}{d\epsilon} \right), \quad (\text{A10})$$

where k_B is the Boltzmann constant, T is the electronic temperature, and $\mathcal{Z} = \text{Tr}(e^{-\hat{H}_{\text{tot}}/k_B T})$ is the partition function. $d\langle n | \hat{n}_R | n \rangle(\epsilon) / d\epsilon$ itself is numerically computed using the central difference method.

[1] E. Rashba and A. L. Efros, Orbital Mechanisms of Electron-Spin Manipulation by an Electric Field, *Phys. Rev. Lett.* **91**, 126405 (2003).
 [2] I. Žutić, J. Fabian, and S. D. Sarma, Spintronics: Fundamentals and applications, *Rev. Mod. Phys.* **76**, 323 (2004).

[3] V. N. Golovach, M. Borhani, and D. Loss, Electric-dipole-induced spin resonance in quantum dots, *Phys. Rev. B* **74**, 165319 (2006).
 [4] R. Hanson, L. P. Kouwenhoven, J. R. Petta, S. Tarucha, and L. M. Vandersypen, Spins in few-electron quantum dots, *Rev. Mod. Phys.* **79**, 1217 (2007).
 [5] S. Nadj-Perge, S. Frolov, E. Bakkers, and L. P. Kouwenhoven, Spin-orbit qubit in a semiconductor nanowire, *Nature* **468**, 1084 (2010).
 [6] K. D. Petersson, L. W. McFaul, M. D. Schroer, M. Jung, J. M. Taylor, A. A. Houck, and J. R. Petta, Circuit quantum electrodynamics with a spin qubit, *Nature* **490**, 380 (2012).
 [7] S. Tarucha, M. Yamamoto, A. Oiwa, B.-S. Choi, and Y. Tokura, in *Principles and Methods of Quantum Information Technologies* (Springer, 2016), p. 541.
 [8] A. Crippa, R. Ezzouch, A. Aprá, A. Amisse, R. Laviéville, L. Hutin, B. Bertrand, M. Vinet, M. Urdampilleta, and T. Meunier, *et al.*, Gate-reflectometry dispersive readout and coherent control of a spin qubit in silicon, *Nat. Commun.* **10**, 1 (2019).
 [9] C. Kloeffel and D. Loss, Prospects for spin-based quantum computing in quantum dots, *Annu. Rev. Condens. Matter Phys.* **4**, 51 (2013).
 [10] A. Chatterjee, P. Stevenson, S. De Franceschi, A. Morello, N. P. de Leon, and F. Kuemmeth, Semiconductor qubits in practice, *Nat. Rev. Phys.* **3**, 157 (2021).
 [11] R. Winkler, S. Papadakis, E. De Poortere, and M. Shayegan, *Spin-Orbit Coupling in Two-Dimensional Electron and Hole Systems* Vol. 41 (Springer, 2003).
 [12] T. Ihn, *Semiconductor Nanostructures: Quantum States and Electronic Transport* (OUP Oxford, 2009).
 [13] J. Kammhuber, M. C. Cassidy, F. Pei, M. P. Nowak, A. Vuik, O. Gul, D. Car, S. Plissard, E. Bakkers, and M. Wimmer, *et al.*, Conductance through a helical state in an indium antimonide nanowire, *Nat. Commun.* **8**, 1 (2017).
 [14] S. Nadj-Perge, V. Pribiag, J. Van den Berg, K. Zuo, S. Plissard, E. Bakkers, S. Frolov, and L. Kouwenhoven, Spectroscopy of Spin-Orbit Quantum Bits in Indium Antimonide Nanowires, *Phys. Rev. Lett.* **108**, 166801 (2012).
 [15] J.-Y. Wang, G.-Y. Huang, S. Huang, J. Xue, D. Pan, J. Zhao, and H. Xu, Anisotropic pauli spin-blockade effect and spin-orbit interaction field in an InAs nanowire double quantum dot, *Nano Lett.* **18**, 4741 (2018).
 [16] S. Dorsch, B. Dalelkhan, S. Fahlvik, and A. Burke, Side-gated, enhancement mode, InAs nanowire double quantum dot devices—toward controlling transverse electric fields in spin-transport measurements, *Nanotechnology* **30**, 144002 (2019).
 [17] R. M. Lutchyn, E. P. Bakkers, L. P. Kouwenhoven, P. Krogstrup, C. M. Marcus, and Y. Oreg, Majorana zero modes in superconductor–semiconductor heterostructures, *Nat. Rev. Mater.* **3**, 52 (2018).
 [18] A. Pfund, I. Shorubalko, K. Ensslin, and R. Leturcq, Spin-state mixing in InAs double quantum dots, *Phys. Rev. B* **76**, 161308 (2007).
 [19] S. Nadj-Perge, S. Frolov, J. Van Tilburg, J. Danon, Y. V. Nazarov, R. Algra, E. Bakkers, and L. Kouwenhoven, Disentangling the effects of spin-orbit and hyperfine interactions on spin blockade, *Phys. Rev. B* **81**, 201305 (2010).
 [20] A. Bogan, S. Studenikin, M. Korkusinski, L. Gaudreau, J. Phoenix, P. Zawadzki, A. Sachrajda, L. Tracy, J. Reno,

- and T. Hargett, Spin-orbit enabled quantum transport channels in a two-hole double quantum dot, *Phys. Rev. B* **103**, 235310 (2021).
- [21] D. Zajac, T. Hazard, X. Mi, E. Nielsen, and J. R. Petta, Scalable Gate Architecture for a One-Dimensional Array of Semiconductor Spin Qubits, *Phys. Rev. Appl.* **6**, 054013 (2016).
- [22] T. Karzig, C. Knapp, R. M. Lutchyn, P. Bonderson, M. B. Hastings, C. Nayak, J. Alicea, K. Flensberg, S. Plugge, and Y. Oreg, *et al.*, Scalable designs for quasiparticle-poisoning-protected topological quantum computation with Majorana zero modes, *Phys. Rev. B* **95**, 235305 (2017).
- [23] J. Colless, A. Mahoney, J. Hornibrook, A. Doherty, H. Lu, A. Gossard, and D. Reilly, Dispersive Readout of a Few-Electron Double Quantum Dot with Fast rf Gate Sensors, *Phys. Rev. Lett.* **110**, 046805 (2013).
- [24] G. Zheng, N. Samkharadze, M. L. Noordam, N. Kalhor, D. Brousse, A. Sammak, G. Scappucci, and L. M. Vandersypen, Rapid gate-based spin read-out in silicon using an on-chip resonator, *Nat. Nanotechnol.* **14**, 742 (2019).
- [25] D. De Jong, J. Van Veen, L. Binci, A. Singh, P. Krogstrup, L. P. Kouwenhoven, W. Pfaff, and J. D. Watson, Rapid Detection of Coherent Tunneling in an InAs Nanowire Quantum Dot Through Dispersive Gate Sensing, *Phys. Rev. Appl.* **11**, 044061 (2019).
- [26] J. Van Veen, D. De Jong, L. Han, C. Prosko, P. Krogstrup, J. D. Watson, L. P. Kouwenhoven, and W. Pfaff, Revealing charge-tunneling processes between a quantum dot and a superconducting island through gate sensing, *Phys. Rev. B* **100**, 174508 (2019).
- [27] D. Sabonis, E. C. O'Farrell, D. Razmadze, D. M. van Zanten, J. Suter, P. Krogstrup, and C. M. Marcus, Dispersive sensing in hybrid InAs/Al nanowires, *Appl. Phys. Lett.* **115**, 102601 (2019).
- [28] D. De Jong, D. Waardenburg, N. Blaznik, L. Han, F. Malinowski, C. Prosko, J. Van Veen, P. Krogstrup, L. Kouwenhoven, and W. Pfaff, Dispersive sensing of electron tunneling between quantum dots in proximitized InAs nanowires, *Bull. Am. Phys. Soc.* **65**, (2020).
- [29] J. Stehlik, Y.-Y. Liu, C. Quintana, C. Eichler, T. Hartke, and J. R. Petta, Fast Charge Sensing of a Cavity-Coupled Double Quantum Dot using a Josephson Parametric Amplifier, *Phys. Rev. Appl.* **4**, 014018 (2015).
- [30] S. Plugge, A. Rasmussen, R. Egger, and K. Flensberg, Majorana box qubits, *New J. Phys.* **19**, 012001 (2017).
- [31] T. B. Smith, M. C. Cassidy, D. J. Reilly, S. D. Bartlett, and A. L. Grimsmo, Dispersive Readout of Majorana Qubits, *PRX Quantum* **1**, 020313 (2020).
- [32] G. Badawy, S. Gazibegovic, F. Borsoi, S. Heedt, C.-A. Wang, S. Koelling, M. A. Verheijen, L. P. Kouwenhoven, and E. P. Bakkers, High mobility stemless InSb nanowires, *Nano Lett.* **19**, 3575 (2019).
- [33] J. Hornibrook, J. Colless, A. Mahoney, X. Croot, S. Blainvilain, H. Lu, A. Gossard, and D. Reilly, Frequency multiplexing for readout of spin qubits, *Appl. Phys. Lett.* **104**, 103108 (2014).
- [34] T. Duty, G. Johansson, K. Bladh, D. Gunnarsson, C. Wilson, and P. Delsing, Observation of Quantum Capacitance in the Cooper-Pair Transistor, *Phys. Rev. Lett.* **95**, 206807 (2005).
- [35] K. Petersson, C. Smith, D. Anderson, P. Atkinson, G. Jones, and D. Ritchie, Charge and spin state readout of a double quantum dot coupled to a resonator, *Nano Lett.* **10**, 2789 (2010).
- [36] W. G. Van der Wiel, S. De Franceschi, J. M. Elzerman, T. Fujisawa, S. Tarucha, and L. P. Kouwenhoven, Electron transport through double quantum dots, *Rev. Mod. Phys.* **75**, 1 (2002).
- [37] A. Cottet, C. Mora, and T. Kontos, Mesoscopic admittance of a double quantum dot, *Phys. Rev. B* **83**, 121311 (2011).
- [38] M. Schroer, M. Jung, K. Petersson, and J. R. Petta, Radio Frequency Charge Parity Meter, *Phys. Rev. Lett.* **109**, 166804 (2012).
- [39] M. Khalil, M. Stoutimore, F. Wellstood, and K. Osborn, An analysis method for asymmetric resonator transmission applied to superconducting devices, *J. Appl. Phys.* **111**, 054510 (2012).
- [40] F. K. Malinowski, L. Han, D. De Jong, J.-Y. Wang, C. G. Prosko, G. Badawy, S. Gazibegovic, Y. Liu, P. Krogstrup, and E. P. Bakkers, *et al.*, Radio-frequency C - V Measurements with Subattofarad Sensitivity, *Phys. Rev. Appl.* **18**, 024032 (2022).
- [41] R. Mizuta, R. Otxoa, A. Betz, and M. F. Gonzalez-Zalba, Quantum and tunneling capacitance in charge and spin qubits, *Phys. Rev. B* **95**, 045414 (2017).
- [42] M. Esterli, R. Otxoa, and M. Gonzalez-Zalba, Small-signal equivalent circuit for double quantum dots at low-frequencies, *Appl. Phys. Lett.* **114**, 253505 (2019).
- [43] A. Bringer, S. Heedt, and T. Schäpers, Dresselhaus spin-orbit coupling in [111]-oriented semiconductor nanowires, *Phys. Rev. B* **99**, 085437 (2019).
- [44] P. Ziesche, O. Gunnarsson, W. John, and H. Beck, Two-site Hubbard model, the Bardeen-Cooper-Schrieffer model, and the concept of correlation entropy, *Phys. Rev. B* **55**, 10270 (1997).
- [45] F. Qu, J. van Veen, F. K. de Vries, A. J. Beukman, M. Wimmer, W. Yi, A. A. Kiselev, B.-M. Nguyen, M. Sokolich, and M. J. Manfra, *et al.*, Quantized conductance and large g -factor anisotropy in InSb quantum point contacts, *Nano Lett.* **16**, 7509 (2016).
- [46] J. Mu, S. Huang, J.-Y. Wang, G.-Y. Huang, X. Wang, and H. Xu, Measurements of anisotropic g -factors for electrons in InSb nanowire quantum dots, *Nanotechnology* **32**, 020002 (2020).
- [47] T. Fujita, P. Stano, G. Allison, K. Morimoto, Y. Sato, M. Larsson, J.-H. Park, A. Ludwig, A. Wieck, and A. Oiwa, *et al.*, Signatures of Hyperfine, Spin-Orbit, and Decoherence Effects in a Pauli Spin Blockade, *Phys. Rev. Lett.* **117**, 206802 (2016).
- [48] T. Lundberg, D. J. Ibberson, J. Li, L. Hutin, J. C. Abadillo-Uriel, M. Filippone, B. Bertrand, A. Nunnenkamp, C.-M. Lee, and N. Stelmashenko, *et al.*, Non-reciprocal Pauli spin blockade in a silicon double quantum dot, (2021), arXiv preprint [ArXiv:2110.09842](https://arxiv.org/abs/2110.09842).
- [49] Z. Scherübl, A. Pályi, G. Frank, I. E. Lukács, G. Fülöp, B. Fülöp, J. Nygård, K. Watanabe, T. Taniguchi, and G. Zaránd, *et al.*, Observation of spin-orbit coupling induced Weyl points in a two-electron double quantum dot, *Commun. Phys.* **2**, 1 (2019).
- [50] V. D. Maman, M. Gonzalez-Zalba, and A. Pályi, Charge Noise and Overdrive Errors in Dispersive Readout of

- Charge, Spin, and Majorana Qubits, [Phys. Rev. Appl. **14**, 064024 \(2020\)](#).
- [51] G. Burkard, D. Loss, and D. P. DiVincenzo, Coupled quantum dots as quantum gates, [Phys. Rev. B **59**, 2070 \(1999\)](#).
- [52] D. Stepanenko, N. E. Bonesteel, D. P. DiVincenzo, G. Burkard, and D. Loss, Spin-orbit coupling and time-reversal symmetry in quantum gates, [Phys. Rev. B **68**, 115306 \(2003\)](#).
- [53] M. Urdampilleta, A. Chatterjee, C. C. Lo, T. Kobayashi, J. Mansir, S. Barraud, A. C. Betz, S. Rogge, M. F. Gonzalez-Zalba, and J. J. Morton, Charge Dynamics and Spin Blockade in a Hybrid Double Quantum Dot in Silicon, [Phys. Rev. X **5**, 031024 \(2015\)](#).